Evolution of physical properties of $RE_3Ni_5Al_{19}$ family (RE = Y, Nd, Sm, Gd, Tb, Dy, Ho, Er)

Zuzanna Ryżyńska[1]*, Madalynn Marshall[2], Weiwei Xie[2], Tomasz Klimczuk[1], Michał J. Winiarski[1†]

[1]*Faculty of Applied Physics and Mathematics and Advanced Materials Centre, Gdansk University of Technology, Narutowicza 11/12, 80-233 Gdansk, Poland*

[2] *Department of Chemistry and Chemical Biology, Rutgers University, Piscataway, NJ 08854, USA*

* zuzanna.sobczak@pg.edu.pl

† michal.winiarski@pg.edu.pl

Single crystals of $RE_3Ni_5Al_{19}$ series (RE = Y, Nd, Sm, Gd, Tb, Dy, Ho Er) were grown using the Al self-flux method. The crystal structure was examined by both single crystal and powder x-ray diffraction. Physical properties were studied for the first time for $RE_3Ni_5Al_{19}$ (RE = Y, Nd, Gd, Tb, Dy, Ho and Er) by means of magnetic susceptibility, electrical resistivity and heat capacity measurements. Complex magnetic behaviors, with up to three transitions present for RE = Sm, Gd, Tb and Dy, were revealed. $Y_3Ni_5Al_{19}$ was found to be a non-magnetic non-superconducting metal (above T = 1.8 K) with weak electron-phonon coupling strength.

I Introduction

The family of $RE_3Ni_5Al_{19}$ was a subject of physical properties studies mostly for the actinides (RE = U, Th) [1–3] and few lanthanides (RE = Sm and Yb) [4,5]. $U_3Ni_5Al_{19}$ was found to be a heavy-fermion antiferromagnet with T_N = 23 K and non-Fermi liquid behavior was observed below 5 K under ambient pressure [1]. Later, strongly interacting fluctuations below T = 0.35 K were revealed in heat capacity of $U_3Ni_5Al_{19}$ [3]. To better understand the behavior of $U_3Ni_5Al_{19}$ and to theoretically examine $Th_3Ni_5Al_{19}$, the ab-initio calculations on structural preferences and phase stability these phases were performed [2]. Low frequency phonon DOS was found to be coming from actinide atoms contribution [2]. Moreover, intermediate valence behavior was found in the Kondo lattice compound $Yb_3Ni_5Al_{19}$ with characteristic energy scale T_K ~ 500 K [4]. In $Sm_3Ni_5Al_{19}$ antiferromagnetic ordering in T = 18 K was observed, and effective magnetic moment calculated from fitting to the Curie-Weiss law was equal to $\mu_{eff} = 2.25\mu_B$ per formula unit [5].

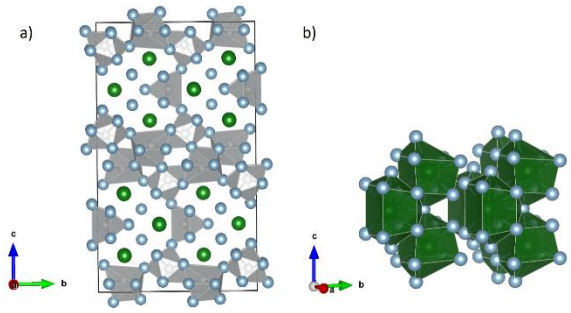

Fig. 1. Crystal structure of $RE_3Ni_5Al_{19}$ compounds. RE, Ni and Al atoms are marked by green, grey and blue balls, respectively. a) Ni-centered cluster b) RE-centered cluster. Images are rendered using VESTA [6].

The crystal structure of $RE_3Ni_5Al_{19}$ shown in Fig. 1, consists of rare earth (RE) atoms coordinated by a pentagonal cluster with five vertexes. Ni atoms are located in trigonal clusters with 3 or 4 vertexes [7,8]. The $RE_3Ni_5Al_{19}$ compounds belong to the family of $RE_{2+m}Ni_{4+m}Al_{15+4m}$ materials [7,8] with orthorhombic (space group *Cmcm*) symmetry for odd "m" and monoclinic one (space group *C2/m*) for even "m" [8]. They are formed with intergrown slabs of monoclinic $RENiAl_4$ (marked with red rectangle in Fig. 2) and hypothetical $RE_2T_4Al_{15}$ cells. The "m" number in $RE_{2+m}Ni_{4+m}Al_{15+4m}$ indicates the quantity of $RENiAl_4$ parts in given compound. So far, only materials with m = 1 ($RE_3Ni_5Al_{19}$) and m = 2 ($RE_4Ni_6Al_{23}$) were reported and structurally characterized.

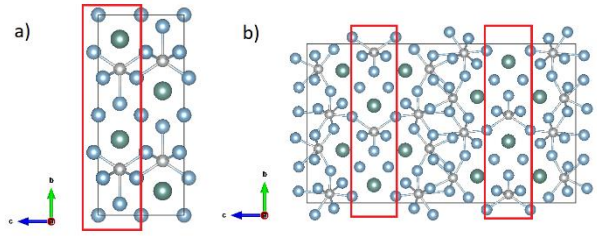

Fig. 2. a) Unit cell of $RENiAl_4$, where RE, Ni and Al are presented as green, grey and blue balls, respectively, b) Unit cell of $RE_3Ni_5Al_{19}$ compound that consists of repeating $RENiAl_4$ slabs (marked with red solid lines) intergrown with $RE_2T_4Al_{15}$ - type slabs. Images rendered using VESTA [6].

Interesting and non-trivial behavior of already known $RE_3Ni_5Al_{19}$ (RE = U, Th, Sm, Yb) compounds inspired us to investigate other rare earth atoms into the structure, which may result in unusual properties of these new materials. In this study we present synthesis and basic study of physical properties for $RE_3Ni_5Al_{19}$ (RE = Y, Nd, Sm, Gd, Tb, Dy, Ho, Er) compounds.

II Materials and Methods

Single crystals of $RE_3Ni_5Al_{19}$ (RE =Y, Nd, Sm, Gd, Tb, Dy, Ho, Er) were grown using the Al self-flux method as described in ref. [9]. Rare-earth metal (pieces, Alfa Aesar, 99.9%), nickel (shot, Alfa Aesar, 99.95%) and aluminum (slug, Alfa Aesar, 99.999%) were put together in an alumina crucible at the atomic ratio of 1:2:40 (RE:Ni:Al) with a frit-disc and a second crucible used for flux separation as proposed by Canfield [10]. The crucibles were put in a quartz tube backfilled with Ar to prevent the Al vapor from attacking the tube walls. The ampoules were then placed in a box furnace, heated to 1000°C, held for 2 hours and then slowly cooled (2°C/h) to 770°C. To separate the crystals from the flux each ampoule was centrifugated at this temperature. The obtained crystals were shiny silver in color and of needle-like shape (Fig. 3).

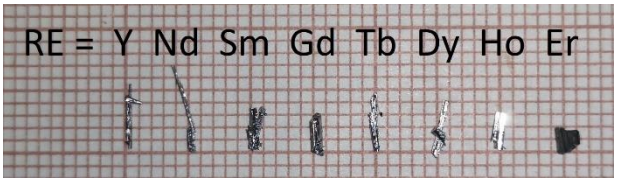

Fig. 3. Single crystals of $RE_3Ni_5Al_{19}$ compounds grown with self-flux method.

The phase identification of obtained crystals was performed with powder x-ray diffraction (PXRD) using Bruker D2 Phaser 2nd generation diffractometer with Cu-Kα radiation and a LynxEye XE-T detector. Single crystal diffraction was used to determine the crystal structure. Crystals were mounted with glycerol on the tips of Kapton loops and the data was collected using Bruker Smart Apex II diffractometer with Mo lamp ($\lambda_{K\alpha}$= 0.71073 Å). 0.5° width of scanning with exposure time of

10 seconds was used to collect the data. To solve the crystal structure SHELXTL software was used [11]. Based on face-index modeling, numerical absorption corrections were approached by XPREP [12].

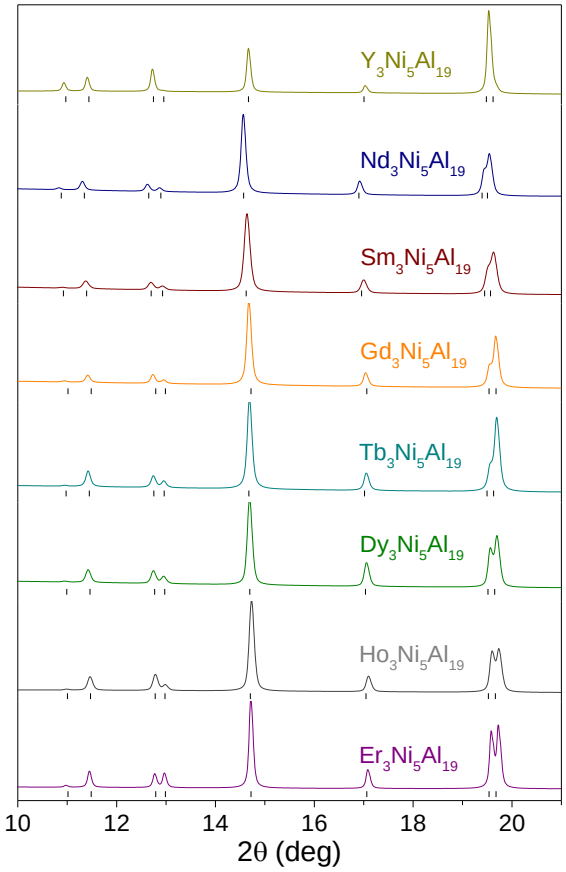

Fig. 4. The X-ray powder diffraction characterization of crushed $RE_3Ni_5Al_{19}$ crystals (RE = Y, Nd, Sm, Gd, Tb, Dy, Ho, Er). Expanded view of the powder pattern showing a shift towards higher angles and a separation of peaks by changing the RE atom. Bragg positions are marked by black ticks.

Physical properties measurements were performed using a Quantum Design Physical Property Measurement System (PPMS) by means of magnetic susceptibility, resistivity and heat capacity measurements in the temperature range 300 K – 1.8 K. Magnetic susceptibility measurements were performed in the dc mode. The zero-field cooled (ZFC) and field cooled (FC) scans were carried out in magnetic fields of 0.5 T and 1 T. Resistivity measurements were performed using a four-probe method with thin Pt wires connected to the crystals with silver paste. A standard 2τ relaxation method was used to measure the heat capacity.

Electronic structure of the model compound $Y_3Ni_5Al_{19}$ was studied using the density functional theory (DFT) calculations. A relaxed model of the structure was taken from the Materials Project database [13,14] and calculations were performed using the ELK full potential linearized augmented plane waves + local orbitals (FP-LAPW+LO) code (ver. 5.2.14) employing the local density approximation (LDA) for the exchange-correlation potential and not accounting for the spin-orbit coupling effects with a k point mesh of 30 x 8 x 5.

III Results

Crystal structure determination was performed by means of a single crystal and powder x-ray diffraction. PXRD scans at room temperature were performed in order to exclude the presence of impurity phases and confirm the crystal structure obtained from single crystal diffraction, and are presented in Fig. 4. All of the observed reflections are indexed into *Cmcm* (no. 63) space group of $Gd_3Ni_5Al_{19}$-type structure. No impurity phases were detected within the resolution of the pXRD (~4%). In low angle range there is a minimal shift of observed peaks towards higher angles (seen e.g. around $2\theta = 15^o$) with increasing atomic number of RE atom in $RE_3Ni_5Al_{19}$. Lattice parameters obtained from the single crystal refinement are presented in Tab. 1 with comparison to those reported previously in the literature. For the rare-earth series $RE_3Ni_5Al_{19}$ the cell volume decreases with increasing atomic number (see Fig. 5), that is consistent with decreasing ionic radius of RE (lanthanide contraction effect). Details of the data obtained from the single-crystal measurements are presented in tables S1-S16 of the Supplementary Information.

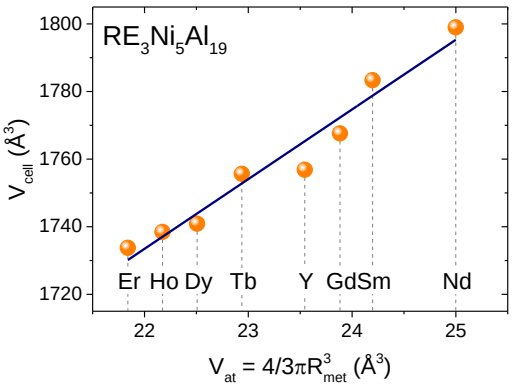

Fig. 5. Cell volume for $RE_3Ni_5Al_{19}$ (RE = Y, Nd, Sm, Gd, Tb, Dy, Ho, Er) series as a function of atomic volume ($V_{at} = 4/3\pi R_{met}^3$, where R_{met} – metallic radius [15]**). Blue line serves as a guide for the eye.**

Full temperature range of *dc* magnetic susceptibility plotted as χ(T) for $RE_3Ni_5Al_{19}$ (RE= Nd, Gd, Tb, Dy, Ho, Er) is presented in figs. S1 of Supplementary Information.

The magnetic susceptibility data shown in main panel of fig. S1 in the SI, measured in $\mu_0 H = 1$ T, were fitted by the Curie-Weiss law $\chi = \chi_0 + \frac{C}{T-\theta_{CW}}$, where C is the Curie constant, θ_{CW} is the Curie-Weiss temperature and χ_0 is the temperature independent contribution to the susceptibility, coming from the sample and sample holder. The Curie constant is used to calculate the effective magnetic moment μ_{eff} using the relation $C = \frac{N_A \mu_B^2 \mu_{eff}^2}{2k_B}$, where N_A is the Avogadro number, μ_B is Bohr

magneton and k_B is Boltzmann constant. The inset of each graph in fig. S1 presents the $1/(\chi-\chi_0)(T)$ plot (χ_0 was taken from the previous fit). Due to the fact that samarium can exhibit both di- and trivalent configuration in intermetallic systems, its valence fluctuations in $Sm_3Ni_5Al_{19}$ precluded successful fitting of the data with the Curie-Weiss law [16]. While in the previous work on this compound by Subbarao et al. [5] the magnetic data were fitted with the modified Curie-Weiss law and gave the magnetic moment of 2.25 μ_B per formula unit, we believe that the assumption of constant magnetic moment of Sm over a broad temperature range is not justified as valence fluctuation are common in Sm-bearing endohedral aluminides [17–20]. The effective magnetic moments calculated from the fits (Tab. 2) are in good agreement with the expected values for RE^{+3} ions. This suggests that the magnetic moment is contributed only by the lanthanide atoms and the spin polarization of the Ni sublattice is negligible (in agreement with *ab initio* calculations [13])

The Curie-Weiss temperatures (θ_{CW}) for $RE_3Ni_5Al_{19}$ (RE = Nd, Gd, Tb, Dy, Ho, Er) series estimated from the fit are gathered in Tab. 3 The values range from θ_{CW} = -45 K to -2.7 K for $Dy_3Ni_5Al_9$ and $Er_3Ni_5Al_9$, respectively and suggest presence of antiferromagnetic fluctuations within paramagnetic state.

Results of physical properties measurements for $Nd_3Ni_5Al_{19}$ are presented in Fig. 6. Panel a) shows the magnetic susceptibility vs. temperature measured in μ_0H = 0.5 T with a transition visible at T = 5.6 K, probably associated with canted antiferromagnetic (AFM) transition. The transition manifests itself as a small change of the normalized resistivity slope as is seen in panel b). There is no visible hysteresis of heating-cooling R(T) curves (not shown here), suggesting the second-order phase transition character. Temperature dependence of the heat capacity data presented in panel c) as C_p/T vs. T shows an anomaly at T = 5.2 K. The anomaly shifts towards lower temperatures with applied magnetic fields. A lambda shape transition confirms second-order character of the anomaly.

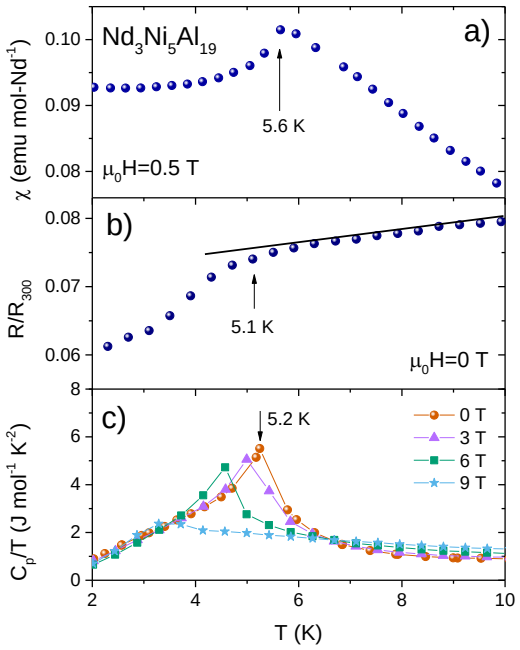

Fig. 6. Results of physical properties measurements for $Nd_3Ni_5Al_{19}$ in low temperature region. a) Magnetic susceptibility as a function of temperature measured in magnetic field μ_0H = 0.5 T, b) Normalized resistance vs. temperature, c) C_p/T vs. T in different applied magnetic fields.

Tab 2. Effective magnetic moment for $RE_3Ni_5Al_{19}$ crystals (RE = Nd, Gd, Tb, Dy, Ho, Er), compared to the expected effective magnetic moments of RE^{+3} ions [21].

RE =	μ_{eff} [μ_B/RE^{3+}] exp.	$\mu_{eff}(RE^{3+})$[μ_B] theory
Nd	3.61(2)	3.62
Gd	7.94(1)	7.94
Tb	9.67(2)	9.72
Dy	10.65(2)	10.63
Ho	10.60(1)	10.60
Er	9.59(1)	9.59

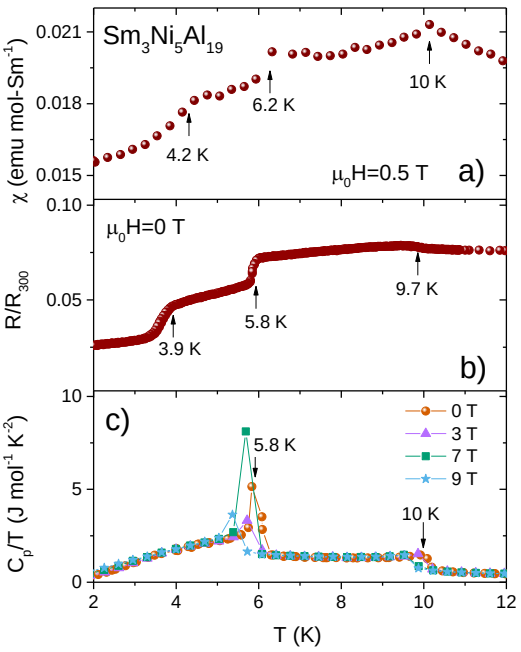

Fig. 7. Results of physical properties measurements for $Sm_3Ni_5Al_{19}$ in low temperature region. a) Magnetic susceptibility as a function of temperature measured in magnetic field μ_0H = 0.5 T, b) Normalized resistance vs. temperature, c) C_p/T vs. T in different applied magnetic fields.

Magnetization, resistivity and heat capacity of $Sm_3Ni_5Al_{19}$ are shown in Fig. 7. Our magnetic and transport results reveal three transitions (in contrary to the AFM transition at 18 K reported in ref. [5]). The three anomalies are visible in magnetic susceptiblity (panel a) and resistivty (panel b) measurements at around 10 K, 6 K and 4 K. Anomalies seen in heat capacity plot (panel c) are visible only at T = 5.9 K and T = 10 K. The transition observed at ca. 4 K in resistivity and magnetization measurements is likely not resolved in the heat capacity measurement due to insufficient resolution. Both anomalies are shifted towards lower temperatures with applied magnetic field, but are still visible in field of 9 T.

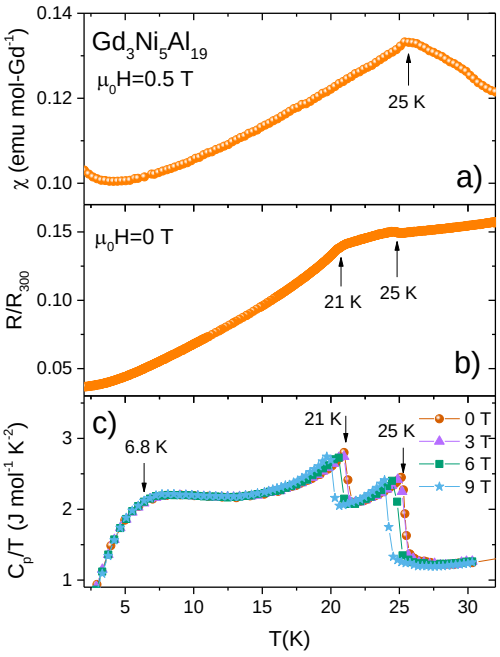

Fig. 8. Results of physical properties measurements for $Gd_3Ni_5Al_{19}$ in low temperature region. a) Magnetic susceptibility as a function of temperature measured in magnetic field μ_0H = 0.5 T, b) Normalized resistance vs. temperature, c) C_p/T vs. T in different applied magnetic fields.

The magnetic susceptibility vs. temperature for $Gd_3Ni_5Al_{19}$ measured in μ_0H = 0.5 T is presented in Fig. 8a). In the data there is a maximum at T = 25 K, that could be interpreted as change to AFM state, followed by slight upturn of the data below T = 3.8 K, most likely coming from the presence of orphan spins and paramagnetic impurities. In case of normalized resistance vs. temperature plot (Fig. 8b) two anomalies are present: T = 25 K and T = 21 K. Heat capacity of $Gd_3Ni_5Al_{19}$ seen in Fig. 7c) exhibits two lambda-shaped transitions at T = 25 K and T = 21 K, as well as a Schottky-like broad hump at T ≈ 7 K, often observed in J = 7/2 systems [22] , similarly to $Sm_3Ni_5Al_{19}$. Two high temperature transitions (T = 25 K and T = 21 K) shift towards lower temperatures with applied magnetic field, while the hump remains unchanged even in field of μ_0H = 9 T.

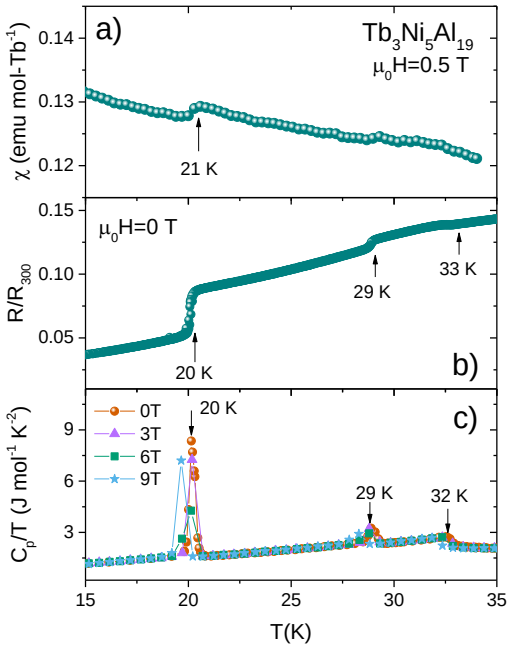

Fig. 9. Results of physical properties measurements in low temperature region for $Tb_3Ni_5Al_{19}$. a) Magnetic susceptibility as a function of temperature measured in magnetic field μ_0H = 0.5 T, b) Normalized resistance vs. temperature, c) C_p/T vs. T in different applied magnetic fields.

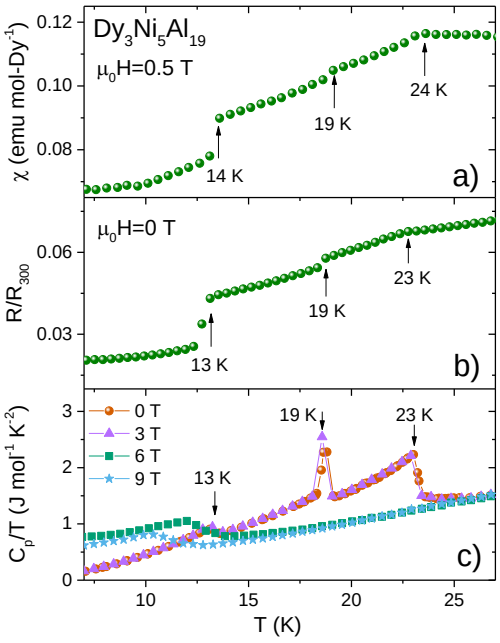

Fig. 10. Results of physical properties measurements for $Dy_3Ni_5Al_{19}$ in low temperature region. a) Magnetic susceptibility as a function of temperature measured in magnetic field μ_0H = 0.5 T, b) Normalized resistance vs. temperature, c) C_p/T vs. T in different applied magnetic fields.

Magnetic susceptibility of $Tb_3Ni_5Al_{19}$ is shown in Fig. 9a). A change of the initial slope is seen at T = 21 K. Normalized resistivity (Fig. 9b) however exhibits three upturns at T = 33 K, T = 29 K, and (the most pronounced) at T = 20 K. Transition at T = 20 K shows hysteretic behavior (shown in detail in fig. S2(a) in the SI) sugessting a first order character transition, while the lack of hysteresis in remaining two is consistent with second-order character. Similarly, in C_p/T vs T plot three anomalies are present at T = 32 K, T = 29 K and T = 20 K. Their temperatures and character is consistent with resistivity results: λ-shape transitions are visible at higher temperatures (T = 32 K and T = 29 K). The anomaly at 20 K is sharp, and heating-cooling curve across the transition (marked as grey area) shows a change of slope (fig. S2b), confirming first order character of the transition [23]. All three anomalies shift towards lower temperatures only with applied field of 9 T.

Results of physical properties measurements for $Dy_3Ni_5Al_{19}$ are presented in Fig. 10. Similarly to $Sm_3Ni_5Al_{19}$, three transitions are visible in magnetic susceptibility measurements (Fig. 9a): at T = 24 K, possibly associated with AFM transition, slight change of the slope at T = 19 K and at T = 14 K. Similarly, in normalized resistance vs. temperature plot (Fig. 9b) upturns at T = 23 K, T = 19 K and T = 13 K are present. Heat capacity results are in agreement with electrical transport and magnetic measurements. Second – order transitions are visible at T = 23 K , T = 19 K, and T = 13 K. With μ_0H = 6 T field applied, two high temperature (T = 23 K and T = 19 K) anomalies disappear, while the third shifts towards lower temperatures.

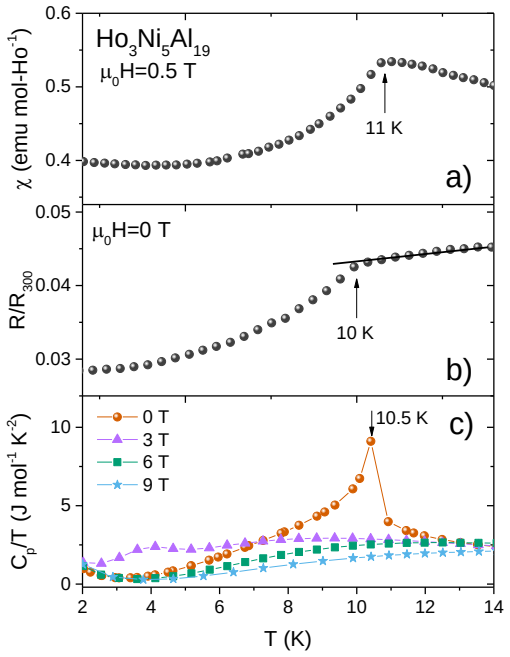

Fig. 11. Results of physical properties measurements for $Ho_3Ni_5Al_{19}$ in low temperature region. a) Magnetic susceptibility as a function of temperature measured in magnetic field μ_0H = 0.5 T, b) Normalized resistance vs. temperature, c) C_p/T vs. T in different applied magnetic fields.

Results for $Ho_3Ni_5Al_{19}$ are shown in Fig. 11. As in $Nd_3Ni_5Al_{19}$ case, only one change of curvature is present for this compound. One, most likely antiferromagnetic transition is seen at T = 11 K in magnetic susceptibility vs. temperature plot (Fig. 10a). Normalized resistance of $Ho_3Ni_5Al_{19}$ (Fig. 10b) exhibits a deviation from linearity at T = 10 K and no hysteresis is observed, suggesting second order phase transition. In case of heat capacity measurements (Fig. 10c) λ-shaped, second-order phase transition is visible at T = 10.5 K.

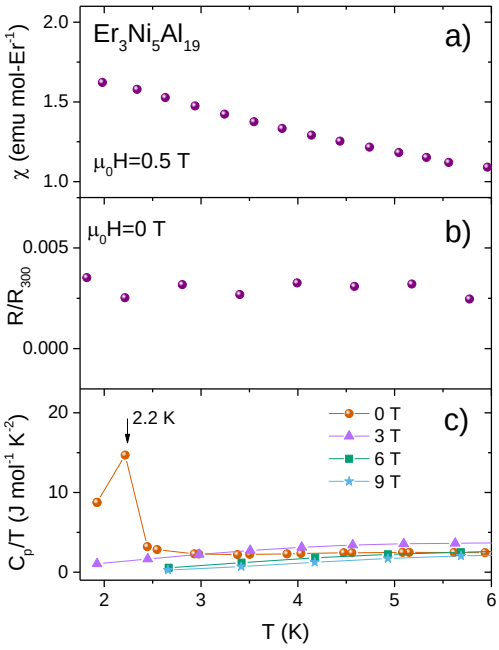

Fig. 12. Results of physical properties measurements in low temperature region for $Er_3Ni_5Al_{19}$. a) Magnetic susceptibility as a function of temperature measured in magnetic field μ_0H = 0.5 T, b) Normalized resistance vs. temperature, c) C_p/T vs. T in different applied magnetic fields.

Fig. 12 shows magnetization, resistivity an heat capacity of $Er_3Ni_5Al_{19}$. No visible transitions or upturns are seen in magnetic susceptibility (Fig. 11a) or normalized resistance (Fig. 11b). An onset of an anomaly is present in heat capacity data (Fig. 11c) at T = 2.2 K.

All of above-described transition temperatures are summarized in Tab. 3. With the exception of the T = 4 K transition of $Sm_3Ni_5Al_{19}$, heat capacity anomalies appear at all the transitions observed in magnetization and resistivity measurements, even if they are not simultaneously observed in both. This is likely due to the fact that both magnetization and resistivity measurement is direction-dependent and the relative orientation of the single crystal with respect to the magnetic field orientation or current flow direction may affect the magnitude of the change in magnetization/resistivity. Heat capacity in turn is a scalar quantity and is only dependent on the entropy changes upon transition. The lack of heat capacity anomaly at T = 4 K in $Sm_3Ni_5Al_{19}$ likely stems from an insufficient measurement resolution and relatively low entropy change at this particular phase transition.

The temperatures of anomalies occurring at the highest temperatures in heat capacity measurements are plotted as a function of deGennes factor in Fig. 13, where g_J is the Lande g-factor and J is the total angular momentum. Purple line serves as a guide for eye. The magnetic transition temperature follows the deGennes scaling for almost all of measured RE in $RE_3Ni_5Al_{19}$, with the exception of Gd. A similar behavior was also observed in the $RENiAl_4$ system

[24]. The deviation may be caused by lack of the orbital contribution to the total angular momentum on Gd^{3+} (S=7/2, L=0). The single ion anisotropy, absent in the case of Gd, plays an important role in formation of the magnetically ordered state in various rare-earth intermetallic systems [25,26].

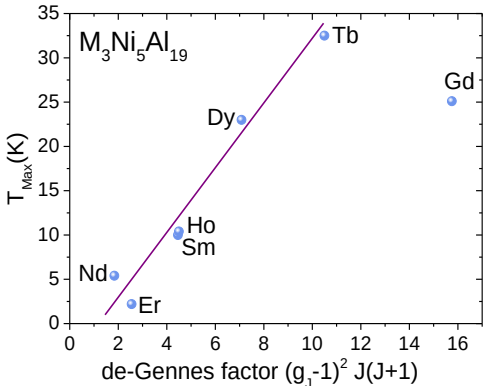

Fig 13. The magnetic order temperature T_{Max} versus deGennes factor for $RE_3Ni_5Al_{19}$ (RE = Nd, Sm, Gd, Tb, Dy, Ho, Er). Purple line serves as a guide for eye.

Nonmagnetic counterpart $Y_3Ni_5Al_{19}$ did not exhibit any transitions in electrical transport measurement (Fig. S3 in the Supplementary Information); the drop of resistance visible at about 170 K results from cracking of the silver epoxy used for fixing the electrical leads). Fig. 14 shows C_p/T vs T^2 in low temperature region of $Y_3Ni_5Al_{19}$. The data was fitted to linear function $C_p/T = \gamma + \beta T^2$, where first term comes from the electronic heat capacity, and second term from lattice heat capacity. The obtained Sommerfeld parameter is γ = 20.6(2) mJ mol^{-1} K^{-2}. The Debye temperature was calculated using the β factor via the relation: $\Theta_D = \sqrt[3]{\frac{12\pi^4 nR}{5\beta_3}}$, where n is number of atoms per formula unit (n = 27) and R is gas constant (R = 8.31 J mol^{-1} K^{-1}). The obtained value is equal to Θ_D = 507(2) K, and is almost 80% higher than the one obtained for $Yb_3Ni_5Al_{19}$ (Θ_D = 282 K) [4], and about 40% higher than for $U_3Ni_5Al_{19}$ (Θ_D = 370 K) [1].

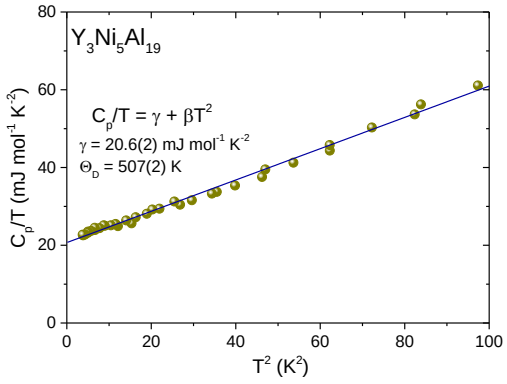

Fig. 14. Low-temperature heat capacity of $Y_3Ni_5Al_{19}$.

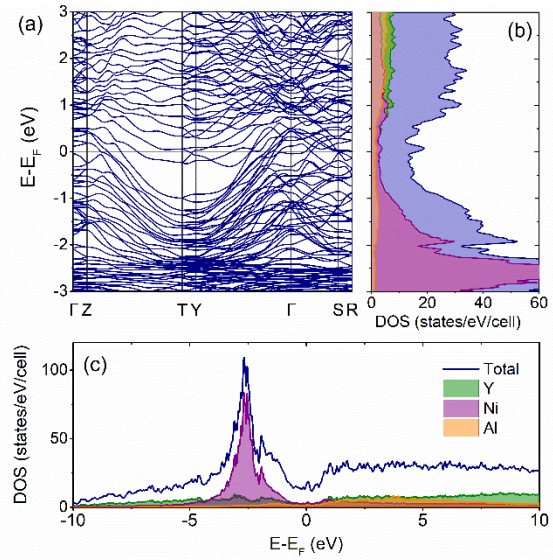

Fig. 15. a) Electronic dispersion curves for $Y_3Ni_5Al_{19}$. A number of flat bands around the Fermi level yield a peak of the DOS just above the E_F (see panel b)). Panel c) shows total DOS with atomic projections. The contribution of Ni 3*d* states is concentrated at around -2.5 eV.

Results of electronic structure calculations for the Y-bearing compound are shown in Fig. 15. Fermi surface within the first Brillouin zone is presented in fig. S4 of Supplementary Information. The band structure and density of states (DOS) function are in qualitative agreement with the results of high-troughput calculations of the Materials Project database [13]. A number of flat bands around E_F result in a peak of DOS just above the E_F. Most of Ni contibution to DOS is found between -5 and -1 eV, consistent with nonmagnetic d^{10} configuration. From the DOS(E_F) one can calculate a "band-structure-only" (i.e. not renormalized by electron-phonon interactions) value of the Sommerfeld coefficient γ_{calc}. Comparison of the calculated and experimental value of γ, gives an estimate of the electron-phonon coupling strength: $\lambda_{ep} = (\gamma_{expt}/\gamma_{calc}) - 1$. With DOS($E_F$) = 8.43 states/eV per formula unit, and γ_{calc} = 19.8 mJ mol^{-1} K^{-2}, this yields $\lambda_{ep} \approx 0.04$, suggesting very weak coupling, in agreement with no superconducting transition being observed down to T = 1.9 K.

IV Conclusions

We have successfully synthesized single crystals of $RE_3Ni_5Al_{19}$ (where RE = Y, Nd, Sm, Gd, Tb, Dy, Ho, Er). Powder x-ray diffraction of crushed crystals confirms the orthorhombic $Gd_3Ni_5Al_{19}$-type structure with *Cmcm* (#63) space group. Magnetic susceptibility, resistivity, and heat capacity measurements revealed complex behavior of all of the studied compounds, except the nonmagnetic $Y_3Ni_5Al_{19}$. Magnetic moment was found to be contributed by rare earth

atoms only. The highest magnetic transition temperatures follow the deGennes scaling with the exception of Gd in $RE_3Ni_5Al_{19}$, which is likely caused by lack of the orbital contribution to the total angular momentum on Gd^{3+} (S=7/2, L=0). Additional local probe measurements and neutron diffraction studies are required to explain the complex magnetic behavior of the $RE_3Ni_5Al_{19}$ series. Low temperature x-ray diffraction may shed light on the detailed character of the first order transition of $Tb_3Ni_5Al_{19}$.

Acknowledgements

The research at Gdańsk Tech was supported by the National Science Centre (Poland) grant (UMO-2018/29/N/ST5/01286). The work at Rutgers University was supported by the U.S. Department of Energy, Office of Science, Basic Energy Sciences, under EPSCoR grant no. DE-SC0012432 with additional support from the Louisiana Board of Regents.

References

[1] E.D. Bauer, V.A. Sidorov, S. Bobev, D.J. Mixson, J.D. Thompson, J.L. Sarrao, M.F. Hundley, High-pressure investigation of the heavy-fermion antiferromagnet $U_3Ni_5Al_{19}$, Phys. Rev. B. 71 (2005) 014419.

[2] J.L. Liu, P. Qian, Y.W. Hu, L.J. Bai, J. Shen, Structural Simulation and Lattice Vibration of $A_3Ni_5Al_{19}$ (A = Th, U), Adv. Mater. Res. (2011).

[3] J.S. Kim, G.R. Stewart, E.D. Bauer, F. Ronning, Unusual temperature dependence in the low-temperature specific heat of $U_3Ni_5Al_{19}$, Phys. Rev. B. 78 (2008) 153108.

[4] E.D. Bauer, S. Bobev, J.D. Thompson, M.F. Hundley, J.L. Sarrao, A. Lobos, A.A. Aligia, Intermediate valence behaviour in the new Kondo lattice compound $Yb_3Ni_5Al_{19}$, J. Phys. Condens. Matter. 16 (2004) 4025.

[5] U. Subbarao, A.K. Ghosh, S. Sarkar, S.C. Peter, Crystal growth, structure and magnetic properties of $Sm_3Ni_5Al_{19}$: A compound in the $Sm_{2n+m}Ni_{4n+m}Al_{15n+4m}$ homologous series, J. Chem. Sci. 126 (2014) 1605–1613.

[6] K. Momma, F. Izumi, VESTA 3 for three-dimensional visualization of crystal, volumetric and morphology data, J. Appl. Crystallogr. 44 (2011) 1272–1276.

[7] S. Delsante, K.W. Richter, H. Ipser, G. Borzone, Synthesis and Structural Characterization of Ternary Compounds Belonging to the Series $RE_{2+m}Ni_{4+m}Al_{15+4m}$ (RE = rare earth metal), Z. Für Anorg. Allg. Chem. 635 (n.d.) 365–368.

[8] R.E. Gladyshevskii, K. Cenzual, E. Parthé, The crystal structure of orthorhombic $Gd_3Ni_5Al_{19}$, a new representative of the structure series $R_{2+m}T_{4+m}Al_{15+4m}$, J. Solid State Chem. 100 (1992) 9–15.

[9] P.C. Canfield, Z. Fisk, Growth of single crystals from metallic fluxes, Philos. Mag. Part B. 65 (1992) 1117–1123.

[10] P.C. Canfield, T. Kong, U.S. Kaluarachchi, N.H. Jo, Use of frit-disc crucibles for routine and exploratory solution growth of single crystalline samples, Philos. Mag. 96 (2016) 84–92.

[11] G.M. Sheldrick, Crystal structure refinement with SHELXL, Acta Crystallogr. Sect. C Struct. Chem. 71 (2015) 3–8.

[12] N. Walker, D. Stuart, An empirical method for correcting diffractometer data for absorption effects, Acta Crystallogr. A. 39 (1983) 158–166.

[13] K. Persson, Materials Data on $Y_3Al_{19}Ni_5$ (SG:63) by Materials Project, (2016).

[14] A. Jain, S.P. Ong, G. Hautier, W. Chen, W.D. Richards, S. Dacek, S. Cholia, D. Gunter, D. Skinner, G. Ceder, K. a. Persson, The Materials Project: A materials genome approach to accelerating materials innovation, APL Mater. 1 (2013) 011002.

[15] K.W. Herrmann, A.H. Daane, F.H. Spedding, *Some physical-metallurgical properties of scandium, yttrium and the rare-earth metals*. United States Atomic Energy Commission, Technical Information Service, 1955

[16] R.B. Beeken, W.R. Savage, J.W. Schweitzer, E.D. Cater, Intermediate valence in $SmSb_xS_{1-x}$ alloys, Phys. Rev. B. 17 (1978) 1334–1339.

[17] A. Sakai, S. Nakatsuji, Strong valence fluctuation effects in $SmTr_2Al_{20}$ (Tr=Ti, V, Cr), Phys. Rev. B. 84 (2011) 201106.

[18] A. Yamada, R. Higashinaka, K. Fushiya, T. Asano, T.D. Matsuda, M. Mizumaki, S. Tsutsui, K. Nitta, T. Ina, T. Uruga, Y. Aoki, Mixed valence states in $(Sm_xLa_{1-x})Tr_2Al_{20}$ (*Tr* = Ti and Ta) studied using X-ray absorption spectroscopy, J. Phys. Conf. Ser. 683 (2016) 012020.

[19] R. Higashinaka, T. Maruyama, A. Nakama, R. Miyazaki, Y. Aoki, H. Sato, Unusual Field-Insensitive Phase Transition and Kondo Behavior in $SmTi_2Al_{20}$, J. Phys. Soc. Jpn. 80 (2011) 093703.

[20] M.W. Wolff, S. Niemann, T. Ebel, W. Jeitschko, Magnetic properties of rare-earth transition metal aluminides $R_6T_4Al_{43}$ with $Ho_6Mo_4Al_{43}$-type structure, J. Magn. Magn. Mater. 223 (2001) 1–15.

[21] J. Jensen, A.R. Mackintosh, Rare earth magnetism: structures and excitations, Clarendon Press, 1991.

[22] D.G. Franco, C. Geibel. *Synthesis an study of the chiral magnetic system $EuIr_2P_2$.* Phys. Rev. B. 104 (2021) 054416.

[23] K. Ramesh Kumar, H.S. Nair, R. Christian, A. Thamizhavel, A.M. Strydom, Magnetic, specific heat and electrical transport properties of Frank-Kasper cage compounds RTM_2Al_{20} [R = Eu, Gd and La; TM = V, Ti], J. Phys. Condens. Matter Inst. Phys. J. 28 (2016) 436002.

[24] B. Saensunon, *A study of the crystal field interaction for two rare earth intermetallic series*. PhD Thesis, University of New South Wales, 2009

[25] P.C. Canfield, Fishing the Fermi sea, Nat. Phys. 4 (2008) 167–169.

[26] L.S. Litzbarski, M.J. Winiarski, T. Klimczuk, M. Łapiński, M. Pugaczowa-Michalska, P. Skokowski, B. Andrzejewski, Intermetallic disordered magnet $Gd_2Pt_{1.1}Ge_{2.9}$ and its relation to other AlB_2-type compounds, Phys. Rev. B 105 (2022) 054427

Tab 1. Crystallographic data for $RE_3Ni_5Al_{19}$ crystals (RE =Y, Nd, Sm, Gd, Tb, Dy, Ho, Er). Cell parameters are obtained from the single crystal refinement.

$RE_3Ni_5Al_{19}$ (RE = Y, Nd, Sm, Gd, Tb, Dy, Ho, Er)						
Space group		*Cmcm* (# 63)				
Pearson symbol		os108				
Number of formula units per cell – *Z*		4				
		Cell parameters (Å)			Cell volume ($Å^3$)	Molar weight (g/mol)
* - *this work*		*a*	*b*	*c*		
$Y_3Ni_5Al_{19}$	*	4.0690(7)	15.963(3)	27.048(4)	1756.86(2)	1072.83
	[5]	4.08	16.04	27.29	1785.94	
$Nd_3Ni_5Al_{19}$	*	4.1143(6)	16.096(2)	27.165(4)	1798.97(4)	1238.83
$Sm_3Ni_5Al_{19}$	*	4.1013(8)	16.035(3)	27.117(5)	1783.33(6)	1257.19
	[5]	4.0974(1)	16.0172(6)	27.0774(10)	1777.06	
$Gd_3Ni_5Al_{19}$	*	4.0863(8)	15.985(3)	27.061(5)	1767.61(4)	1277.86
	[8]	4.08	15.99	27.09	1767.33	
$Tb_3Ni_5Al_{19}$	*	4.0758(8)	15.948(3)	27.010(5)	1755.67(3)	1282.89
	[5]	4.035	15.91	27.08	1738.45	
$Dy_3Ni_5Al_{19}$	*	4.0555(4)	15.891(2)	27.014(3)	1740.9(9)	1293.61
	[5]	4.021	15.86	27.01	1722.51	
$Ho_3Ni_5Al_{19}$	*	4.0584(10)	15.896(4)	26.948(7)	1738.48(2)	1300.90
	[5]	3.991	15.75	26.92	1692.14	
$Er_3Ni_5Al_{19}$	*	4.0550(8)	15.862(4)	26.955(6)	1733.76(2)	1307.89
	[5]	3.960	15.63	26.81	1659.40	

Table 3 Curie-Weiss and the anomaly temperature values visible in magnetic susceptibility, resistivity and heat capacity measurements for $RE_3Ni_5Al_{19}$ (RE = Y, Nd, Sm, Gd, Tb, Dy, Ho, Er)

	Transition temperatures [K] for $RE_3Ni_5Al_{19}$, RE =														
	Y	Nd	Sm			Gd		Tb			Dy			Ho	Er
Θ_{CW}	-	-5(2)	-			-26.9(8)		-37.7(8)			-45(1)			-13.2(5)	-2.7(3)
χ(T)	-	5.6	4.2	6.2	10		25	21			14	19	24	11	-
R(T)	-	5.1	3.9	5.8	9.7	21	25	20	29	33	13	19	23	10	-
C_p(T)	-	5.2	-	5.8	10	21	25	20	29	32	13	19	23	10.5	2.2

Evolution of physical properties of $RE_3Ni_5Al_{19}$ family (RE = Y, Nd, Sm, Gd, Tb, Dy, Ho, Er) – Supplementary Information

Zuzanna Ryżyńska[1]*, Weiwei Xie[2], Tomasz Klimczuk[1], Michał J. Winiarski[1†]

[1]*Faculty of Applied Physics and Mathematics, Gdansk University of Technology, Narutowicza 11/12, 80-233 Gdansk, Poland*

[2]*Department of Chemistry, Louisiana State University, Baton Rouge, LA, USA 70803*

* zuzanna.sobczak@pg.edu.pl

† michal.winiarski@pg.edu.pl

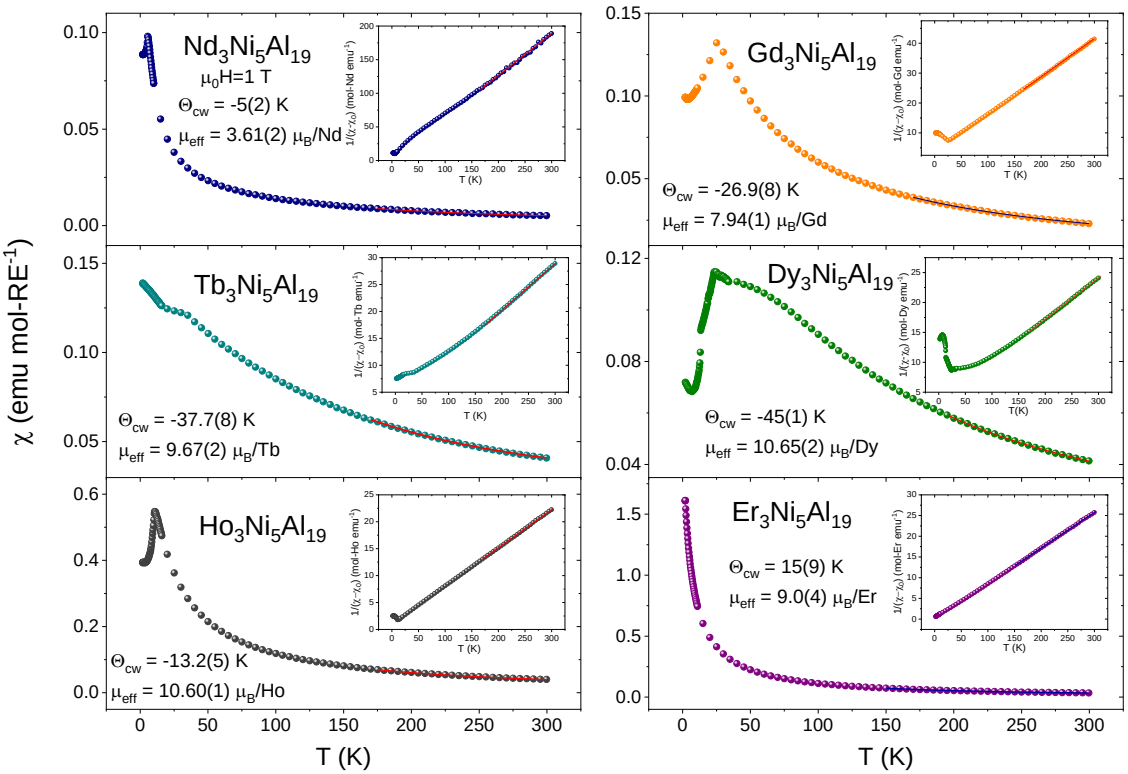

Fig. S1. Main Panel: magnetic susceptibility vs. temperature in 1.9 – 300 K range, fitted to the Curie-Weiss law in high temperature region for $RE_3Ni_5Al_{19}$ (RE = Nd, Gd, Tb, Dy, Ho, Er). Inset: Reciprocal magnetic susceptibility in the temperature range of 1.9 – 300 K and fit to the inverted Curie-Weiss law.

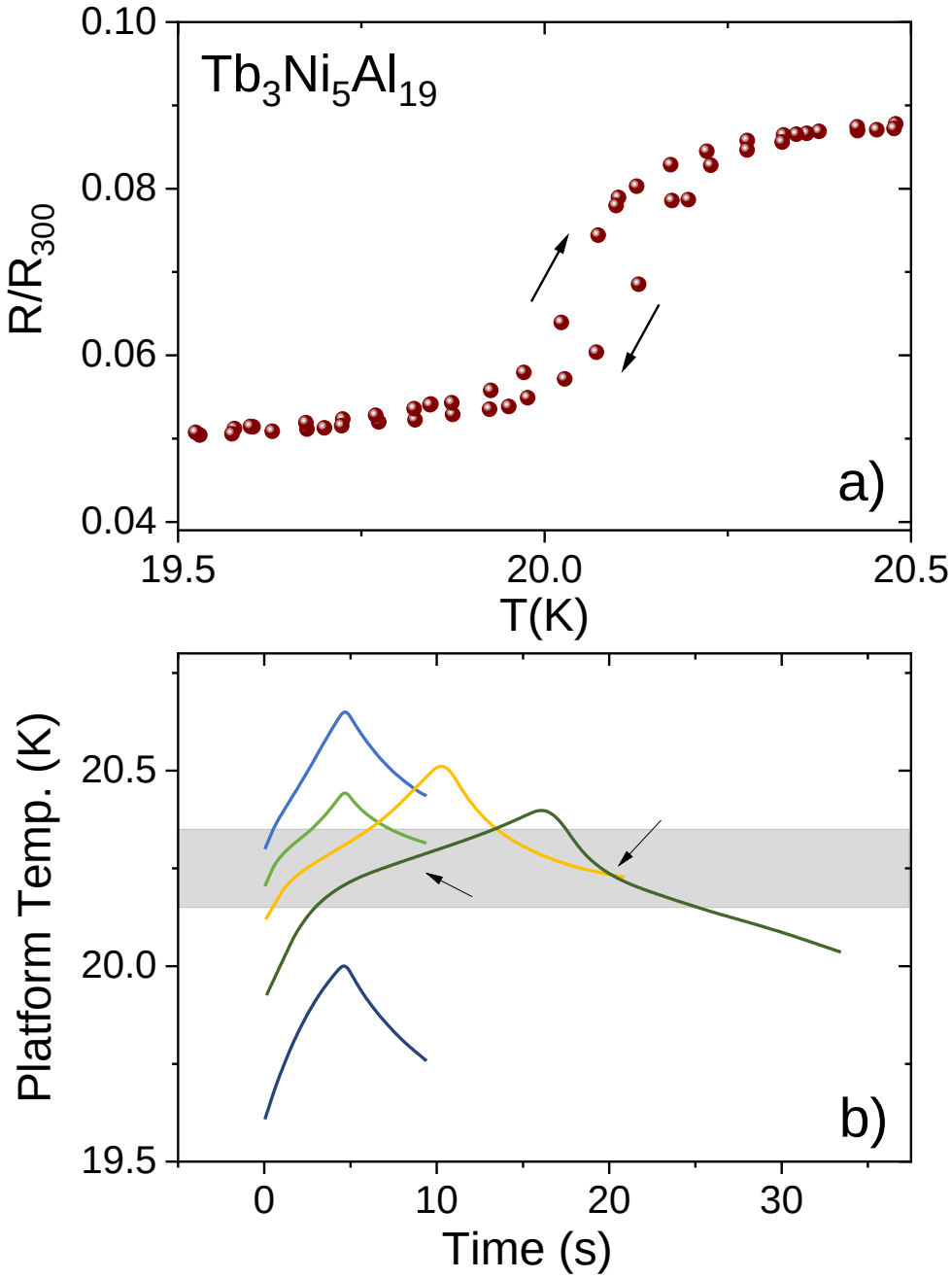

Fig. S2. Confirmation of first order character of T ≈ 20 K transition for $Tb_3Ni_5Al_{19}$. a) Hysteretic behavior of normalized resistance, b) Heating-cooling curves across transition at T ≈ 20 K (grey area) for $Tb_3Ni_5Al_{19}$. Discontinuity caused by first order transition in grey area is marked with arrows.

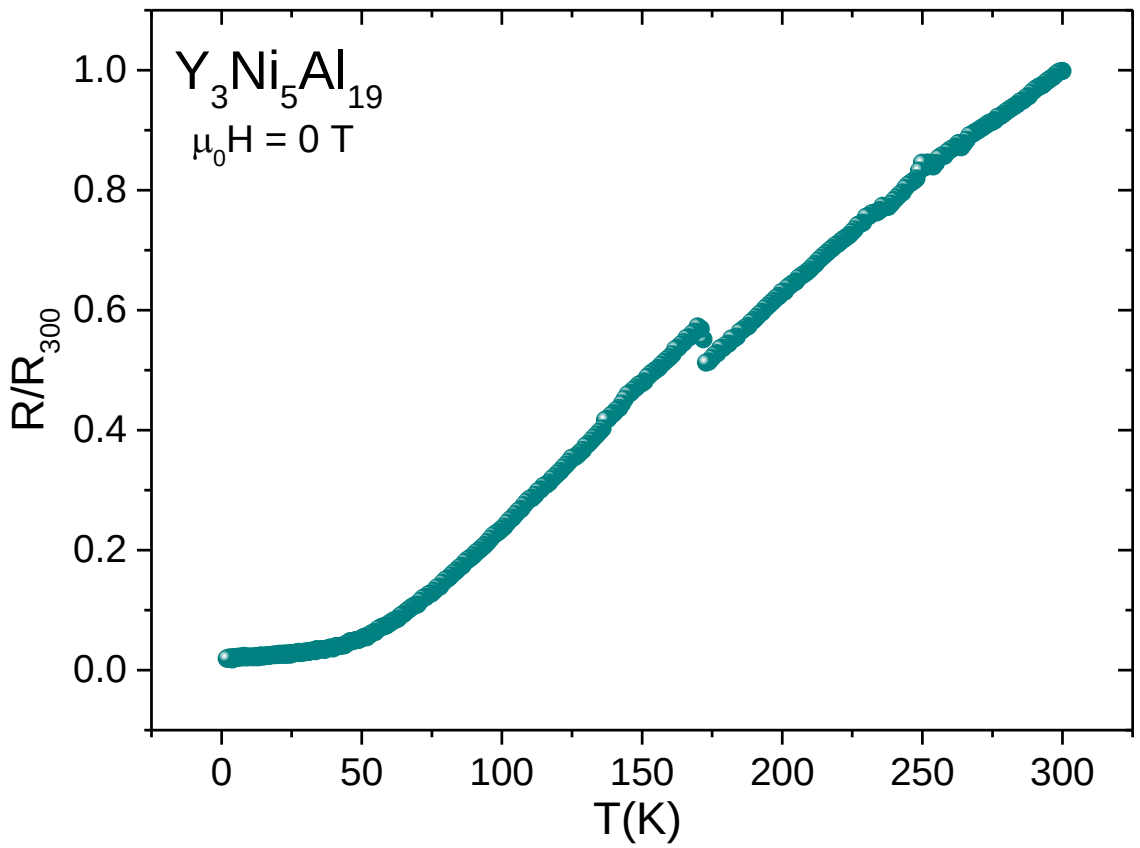

Fig. S3. Results of electrical transport measurement for $Y_3Ni_5Al_{19}$. Change of resistance visible at about 170 K comes from measurements faults.

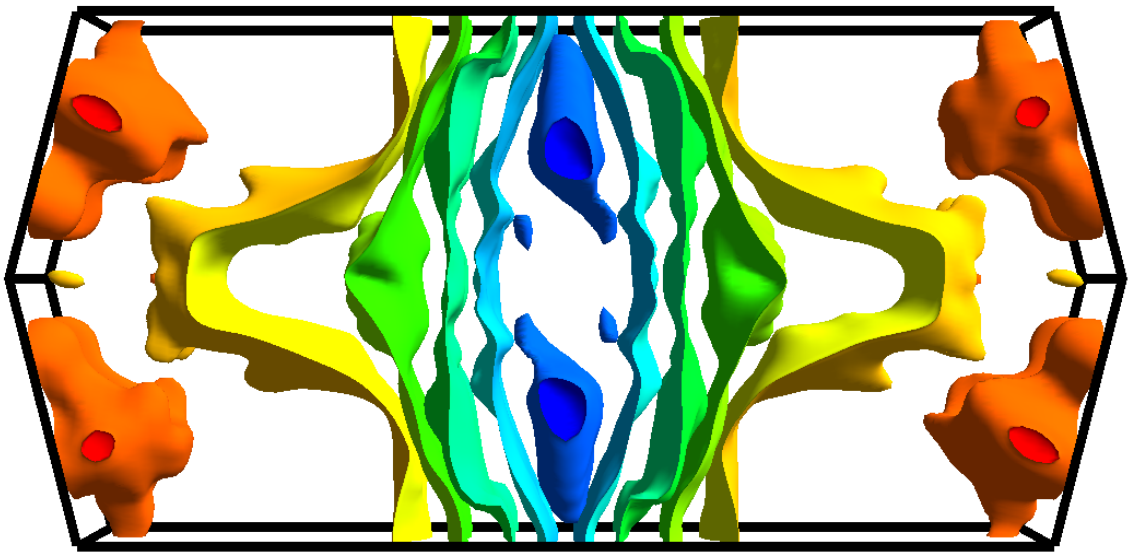

Fig. S4. Fermi surface of $Y_3Ni_5Al_{19}$ within the first Brillouin zone with a total of 12 individual bands crossing the E_F.

Table S1 Single crystal crystallographic data for $Y_3Ni_5Al_{19}$

Refined Formula	$Y_3Ni_5Al_{19}$
a(Å)	4.0690(7)
b(Å)	15.963(3)
c(Å)	27.048(4)
Extinction coefficient	0.00095(10)
Θ range (deg)	1.506-33.245
hkl ranges	$-6 \le h \le 6$ $-24 \le k \le 17$ $-41 \le l \le 29$
No. reflections; R_{int}	1914; 0.0265
No. independent reflections	1710
No. parameters	86
R_1: ωR_2 (all *I*)	0.0203; 0.0516
Goodness of fit	1.221
Diffraction peak and hole (e^-/ Å^3)	0.913; -0.800

Table S2 Atomic coordinates and equivalent isotropic displacement parameters from single crystal refinement of $Y_3Ni_5Al_{19}$ crystals

Atom	**Wyckoff.**	**Occ.**	***x***	***y***	***z***	U_{eq}
Y1	*4c*	1	0	0.38833(3)	0.25	0.00488(11)
Y2	*8f*			0.16609(2)	0.13513(2)	0.00487(10)
Ni1	*4c*			0.04516(4)	0.25	0.00485(14)
Ni2	*8f*			0.34107(3)	0.54247(2)	0.00441(11)
Ni3				0.05388(3)	0.58462(2)	0.00579(12)
Al1	*4c*			0.19377(12)	0.25	0.0075(3)
Al2	*8f*			0.53650(8)	0.10106(5)	0.0063(2)
Al3				0.03567(8)	0.67438(5)	0.0076(2)
Al4				0.57935(8)	0.20179(5)	0.0076(2)
Al5				0.36987(8)	0.13533(5)	0.0077(2)
Al6				0.23436(8)	0.02864(5)	0.0065(2)
Al7				0.06716(8)	0.03136(5)	0.0072(2)

Al8	0.20892(8)	0.58880(4)	0.0063(2)
Al9	0.22390(8)	0.69360(4)	0.0081(2)
Al10	0.40558(9)	0.03691(5)	0.0083(2)

Table S3 Single crystal crystallographic data for $Nd_3Ni_5Al_{19}$

Refined Formula	**$Nd_3Ni_5Al_{19}$**
a(Å)	4.1143(6)
b(Å)	16.096(2)
c(Å)	27.165(4)
Extinction coefficient	0.00090(3)
Θ range (deg)	1.499-33.749
hkl ranges	$-6 \le h \le 6$ $-24 \le k \le 24$ $-42 \le l \le 41$
No. reflections; R_{int}	2044; 0.0177
No. independent reflections	1898
No. parameters	86
R_1: ωR_2 (all *I*)	0.0151; 0.0279
Goodness of fit	1.306
Diffraction peak and hole (e^-/ Å^3)	0.834; -1.400

Table S4 Atomic coordinates and equivalent isotropic displacement parameters from single crystal refinement of $Nd_3Ni_5Al_{19}$ crystals

Atom	**Wyckoff.**	**Occ.**	***x***	***y***	***z***	U_{eq}
Nd1	*4c*			0.38570(2)	0.25	0.00531(4)
Nd2	*8f*			0.16574(2)	0.13506(2)	0.00490(4)
Ni1	*4c*			0.04490(3)	0.25	0.00577(9)
Ni2	*8f*	1	0	0.34024(2)	0.54156(2)	0.00510(6)
Ni3				0.05286(2)	0.58293(2)	0.00657(7)
Al1	*4c*			0.19217(7)	0.25	0.0085(2)
Al2	*8f*			0.53593(5)	0.09949(3)	0.00747(15)
Al3				0.03533(5)	0.67306(3)	0.00870(16)

Al4		0.57694(6)	0.20182(3)	0.00826(16)
Al5		0.37028(5)	0.13439(3)	0.00876(16)
Al6		0.23447(5)	0.02815(3)	0.00719(15)
Al7		0.06811(5)	0.02984(3)	0.00781(15)
Al8		0.20793(5)	0.58788(3)	0.00716(15)
Al9		0.22442(6)	0.69286(3)	0.00937(16)
Al10		0.40452(5)	0.03710(3)	0.00871(16)

Table S5 Single crystal crystallographic data for $Sm_3Ni_5Al_{19}$

Refined Formula	**$Sm_3Ni_5Al_{19}$**
a(Å)	4.1013(8)
b(Å)	16.035(3)
c(Å)	27.117(5)
Extinction coefficient	0.00095(3)
Θ range (deg)	2.540-36.463
hkl ranges	$-6 \le h \le 5$ $-26 \le k \le 26$ $-45 \le l \le 44$
No. reflections; R_{int}	2455; 0.0319
No. independent reflections	2095
No. parameters	86
R_1: ωR_2 (all *I*)	0.0224; 0.0348
Goodness of fit	1.058
Diffraction peak and hole (e^-/ Å^3)	1.051; -1.474

Table S6 Atomic coordinates and equivalent isotropic displacement parameters from single crystal refinement of $Sm_3Ni_5Al_{19}$ crystals

Atom	**Wyckoff.**	**Occ.**	***x***	***y***	***z***	U_{eq}
Sm1	*4c*	1	0	0.38639(2)	0.25	0.00469(5)
Sm2	*8f*			0.16592(2)	0.13520(2)	0.00458(4)
Ni1	*4c*			0.04513(4)	0.25	0.00528(11)
Ni2	*8f*			0.34056(2)	0.54189(2)	0.00474(8)

Ni3		0.05319(3)	0.58360(2)	0.00621(8)
Al1	*4c*	0.19291(9)	0.25	0.0080(3)
Al2		0.53629(6)	0.10018(4)	0.00667(19)
Al3		0.03552(6)	0.67377(4)	0.0082(2)
Al4		0.57793(7)	0.20186(4)	0.0078(2)
Al5		0.37014(6)	0.13476(4)	0.00818(19)
Al6	*8f*	0.23454(6)	0.02842(4)	0.00687(19)
Al7		0.06785(6)	0.03041(4)	0.00723(19)
Al8		0.20843(6)	0.58833(4)	0.00711(19)
Al9		0.22428(7)	0.69316(4)	0.00840(19)
Al10		0.40512(7)	0.03709(4)	0.0084(2)

Table S7 Single crystal crystallographic data for $Gd_3Ni_5Al_{19}$

Refined Formula	**$Gd_3Ni_5Al_{19}$**
a(Å)	4.0863(8)
b(Å)	15.985(3)
c(Å)	27.061(5)
Extinction coefficient	0.000447(19)
Θ range (deg)	1.505-45.389
hkl ranges	$-8 \le h \le 7$ $-31 \le k \le 32$ $-54 \le l \le 53$
No. reflections; R_{int}	4105; 0.0401
No. independent reflections	3369
No. parameters	86
R_1: ωR_2 (all *I*)	0.0254; 0.0365
Goodness of fit	1.088
Diffraction peak and hole (e^-/ Å^3)	1.781; -2.443

Table S8 Atomic coordinates and equivalent isotropic displacement parameters from single crystal refinement of $Gd_3Ni_5Al_{19}$ crystals

Atom	Wyckoff.	Occ.	*x*	*y*	*z*	U_{eq}
Gd1	*4c*			0.38714(2)	0.25	0.00489(4)
Gd2	*8f*			0.16603(2)	0.13522(2)	0.00482(3)
Ni1	*4c*			0.04516(4)	0.25	0.00528(9)
Ni2	*8f*			0.34076(2)	0.54211(2)	0.00464(6)
Ni3				0.05353(3)	0.58413(2)	0.00607(7)
Al1	*4c*			0.19321(9)	0.25	0.0077(2)
Al2	*8f*	1	0	0.53650(6)	0.10068(4)	0.00657(16)
Al3				0.03550(7)	0.67405(4)	0.00806(17)
Al4				0.57845(7)	0.20175(4)	0.00757(17)
Al5				0.36981(7)	0.13497(4)	0.00813(17)
Al6				0.23438(7)	0.02855(4)	0.00684(17)
Al7				0.06747(7)	0.03084(4)	0.00764(17)
Al8				0.20875(6)	0.58860(4)	0.00699(17)
Al9				0.22412(7)	0.69334(4)	0.00831(17)
Al10				0.40558(7)	0.03707(4)	0.00832(17)

Table S9 Single crystal crystallographic data for $Tb_3Ni_5Al_{19}$

Refined Formula	**$Tb_3Ni_5Al_{19}$**
a(Å)	4.0758(8)
b(Å)	15.948(3)
c(Å)	27.010(5)
Extinction coefficient	0.000145(12)
Θ range (deg)	1.508-36.344
hkl ranges	$-6 \le h \le 6$ $-26 \le k \le 16$ $-45 \le l \le 38$

No. reflections; R_{int}	2405; 0.0502
No. independent reflections	1886
No. parameters	86
R_1: ωR_2 (all I)	0.0296; 0.0406
Goodness of fit	0.989
Diffraction peak and hole (e^-/ Å^3)	2.078; -2.042

Table S10 Atomic coordinates and equivalent isotropic displacement parameters from single crystal refinement of $Tb_3Ni_5Al_{19}$ crystals

Atom	Wyckoff.	Occ.	*x*	*y*	*z*	U_{eq}
Tb1	*4c*			0.38750(2)	0.25	0.00531(7)
Tb2	*8f*			0.16612(2)	0.13528(2)	0.00488(5)
Ni1	*4c*			0.04531(6)	0.25	0.00543(16)
Ni2	*8f*			0.34092(4)	0.54230(2)	0.00464(11)
Ni3				0.05371(4)	0.58449(2)	0.00599(12)
Al1	*4c*			0.19340(15)	0.25	0.0081(4)
Al2	*8f*	1	0	0.53691(10)	0.10105(6)	0.0065(3)
Al3				0.03553(11)	0.67426(6)	0.0085(3)
Al4				0.57893(11)	0.20177(6)	0.0079(3)
Al5				0.36974(11)	0.13524(6)	0.0082(3)
Al6				0.23455(11)	0.02875(5)	0.0066(3)
Al7				0.06725(10)	0.03118(6)	0.0071(3)
Al8				0.20924(10)	0.58873(5)	0.0067(3)
Al9				0.22424(11)	0.69349(5)	0.0080(3)
Al10				0.40589(11)	0.03705(6)	0.0080(3)

Table S11 Single crystal crystallographic data for $Dy_3Ni_5Al_{19}$

Refined Formula	**$Dy_3Ni_5Al_{19}$**
a(Å)	4.0555(12)
b(Å)	15.891(5)
c(Å)	27.014(7)
Extinction coefficient	0.00019(3)
Θ range (deg)	1.508 - 33.210
hkl ranges	$-6 \le h \le 6$ $-24 \le k \le 24$ $-41 \le l \le 38$
No. reflections; R_{int}	9432; 0.1796
No. independent reflections	1904
No. parameters	86
R_1: ωR_2 (all *I*)	0.0542; 0.0819
Goodness of fit	0.983
Diffraction peak and hole (e^-/ Å^3)	3.842; -2.590

Table S12 Atomic coordinates and equivalent isotropic displacement parameters from single crystal refinement of $Dy_3Ni_5Al_{19}$ crystals

Atom	**Wyckoff.**	**Occ.**	***x***	***y***	***z***	U_{eq}
Dy1	*4c*	1	0	0.38789(6)	0.25	0.008(1)
Dy2	*8f*			0.16628(4)	0.13529(3)	0.007(1)
Ni1	*4c*			0.04516(17)	0.25	0.008(1)
Ni2	*8f*			0.05404(12)	0.58473(7)	0.009(1)
Ni3				0.34117(12)	0.54256(7)	0.008(1)
Al1	*4c*			0.1943(4)	0.25	0.011(1)
Al2	*8f*			0.0362(3)	0.67453(17)	0.008(1)
Al3				0.0672(3)	0.03160(17)	0.007(1)
Al4				0.2093(3)	0.58901(16)	0.007(1)
Al5				0.2240(3)	0.69358(17)	0.010(1)
Al6				0.2340(3)	0.02853(17)	0.010(1)

Al7		0.3694(3)	0.13532(18)	0.009(1)
Al8		0.4054(3)	0.03715(18)	0.011(1)
Al9		0.5371(3)	0.10143(16)	0.007(1)
Al10		0.5796(3)	0.20151(18)	0.011(1)

Table S13 Single crystal crystallographic data for $Ho_3Ni_5Al_{19}$

Refined Formula	**$Ho_3Ni_5Al_{19}$**
a(Å)	4.0584(10)
b(Å)	15.896(4)
c(Å)	26.948(7)
Extinction coefficient	0.00069(4)
Θ range (deg)	1.511-30.541
hkl ranges	$-5 \le h \le 5$ $-22 \le k \le 12$ $-38 \le l \le 34$
No. reflections; R_{int}	1536; 0.0212
No. independent reflections	1411
No. parameters	101
R_1: ωR_2 (all *I*)	0.0177; 0.0369
Goodness of fit	1.367
Diffraction peak and hole (e^-/ Å^3)	1.054; -0.821

Table S14 Atomic coordinates and equivalent isotropic displacement parameters from single crystal refinement of $Ho_3Ni_5Al_{19}$ crystals

Atom	**Wyckoff.**	**Occ.**	***x***	***y***	***z***	U_{eq}
Ho1	*4c*			0.38847(2)	0.25	0.00581(10)
Ho2	*8f*			0.16621(2)	0.13527(2)	0.00605(7)
Ni1	*4c*			0.04544(5)	0.25	0.0050(3)
Ni2	*8f*	1	0	0.34115(4)	0.54258(2)	0.00658(18)
Ni3				0.05403(4)	0.58498(2)	0.00753(19)
Al1	*4c*			0.19414(13)	0.25	0.0043(6)
Al2	*8f*			0.53683(9)	0.10136(5)	0.0075(4)

Al3		0.03571(9)	0.67457(5)	0.0054(5)
Al4		0.57999(10)	0.20174(5)	0.0058(5)
Al5		0.36931(10)	0.13545(5)	0.0070(5)
Al6		0.23443(9)	0.02874(5)	0.0102(4)
Al7		0.06689(9)	0.03160(6)	0.0105(4)
Al8		0.20940(9)	0.58905(5)	0.0087(5)
Al9		0.22392(10)	0.69375(5)	0.0056(5)
Al10		0.40621(10)	0.03712(6)	0.0119(5)

Table S15 Single crystal crystallographic data for $Er_3Ni_5Al_{19}$

Refined Formula	**$Er_3Ni_5Al_{19}$**
a(Å)	4.0550(8)
b(Å)	15.862(4)
c(Å)	26.955(6)
Extinction coefficient	0.00031(7)
Θ range (deg)	1.511-33.438
hkl ranges	$-5 \le h \le 6$ $-24 \le k \le 22$ $-41 \le l \le 21$
No. reflections; R_{int}	1923; 0.0674
No. independent reflections	1425
No. parameters	55
R_1: ωR_2 (all *I*)	0.0415; 0.1103
Goodness of fit	0.831
Diffraction peak and hole (e^-/ Å^3)	3.305; -2.600

Table S16 Atomic coordinates and equivalent isotropic displacement parameters from single crystal refinement of $Er_3Ni_5Al_{19}$ crystals

Atom	**Wyckoff.**	**Occ.**	***x***	***y***	***z***	U_{eq}
Er1	*4c*			0.38898(5)	0.25	0.0065(2)
Er2	*8f*	1	0	0.16631(3)	0.13521(2)	0.00705(16)
Ni1	*4c*			0.04574(14)	0.25	0.0064(6)

Ni2	*8f*	0.34127(10)	0.54277(5)	0.0085(4)
Ni3		0.05408(10)	0.58524(5)	0.0087(4)
Al1	*4c*	0.1947(4)	0.25	0.0051(10)
Al2		0.5368(2)	0.10170(13)	0.0098(10)
Al3		0.0356(2)	0.67472(13)	0.0061(8)
Al4		0.5807(4)	0.20152(14)	0.0065(8)
Al5		0.3690(4)	0.13567(13)	0.0083(11)
Al6	*8f*	0.2342(2)	0.02905(13)	0.0116(10)
Al7		0.0666(4)	0.03180(14)	0.0162(10)
Al8		0.2097(2)	0.58925(13)	0.0112(10)
Al9		0.2237(4)	0.69389(13)	0.0061(8)
Al10		0.4063(4)	0.03712(14)	0.0151(11)